LES of additive and non-additive pulsatile flows in a model arterial stenosis

Md. Mamun Molla[1], Manosh C. Paul[1] *and Giles Roditi[2]
[1]Department of Mechanical Engineering, University of Glasgow, Glasgow G12 8QQ, UK
[2]Department of Radiology, Glasgow Royal Infirmary, 16 Alexandra parade, Glasgow G31 2ER, UK

Abstract

Transition of additive and non-additive pulsatile flows through a simple 3D model of arterial stenosis is investigated by using a Large Eddy Simulation (LES) technique. We find in both the pulsatile cases that the interaction of the two shear layers, one of which separates from the nose of the stenosis and the another one from its opposite wall, causes recirculation in the flow downstream of the stenosis where the nature of the transient flow becomes turbulent. The strength of this recirculation is found quite high from the non-additive pulsations when the flow Reynolds numbers, $Re \geq 1500$, for which both the pressure and shearing stresses take on an oscillating form at the post stenotic region. Potential medical consequences of these results are discussed in the paper. In addition, some comparisons of the non-additive pulsatile results are given with those of both the additive pulsatile and steady flows. The capability of using LES to simulate the pulsatile transitional flow is also assessed, and the present results show that the SGS contributes about 78% energy dissipation to the flow when the Reynolds number is taken as 2000. The level of SGS dissipation decreases as the Reynolds number is decreased. The numerical results are validated with the experimental data available in literature where a quite good agreement is found.

Keywords: Pulsatile flow modelling, Arterial stenosis, Transition to turbulent flow, Large Eddy Simulation.

*E-mail:m.paul@mech.gla.ac.uk, Tel:+44 (0)141 330 8466, Fax:+44 (0)141 330 4343

1 Introduction

The term arterial stenosis refers to narrowing of an artery in which the cross-sectional area of an artery reduces. The most common cause is atherosclerosis where cholesterol and other lipids are left beneath the intima (inner lining) of the arterial wall. As the amount of this fatty material increases there is an accompanying proliferation of connective tissue and the whole forms a thickened area in the vessel wall called plaque. The arterial wall reshapes itself to accommodate the varying degrees of cross-sectional area of an artery and retard blood flow. When the reduction in arterial calibre is severe, the result is that blood flow takes transition to turbulent with a pressure drop across the stenotic region. The alteration in flow dynamics in turn produces abnormal wall shear stress both at the plaque and at the post stenotic region such that the plaque may fissure and rupture exposing the lipid plaque core to the blood stream with potential for thrombosis (blood clotting) at the site of rupture. This development of atherothrombosis may dangerously acutely occlude the vessel with, in critical territories such as the coronary arteries and cerebral vessels, potentially catastrophic results. Non-occlusive atherotrhombosis is also clinically important as the thrombotic material deposited is often unstable and a source of distal embolism, this is particularly important in the extracranial carotid arteries as a source of stroke.

Interestingly it is the sites of low wall shear stress that are prone to these lipid accumulations and hence plaque formation, Malek *et al.* [1], this is thought to be through stimulating an atherogenic phenotype in the cells of the endothelium (vessel lining). Furthermore, it is the pulsatile nature of flow and the oscillatory shear index that is increasingly being recognised as the important factor in this process as has been shown in 4D MRI experiments, Frydrychowicz *et al.* [2]. The blood flow through arteries is inherently unsteady due to the cyclic nature of heart pump. These disturbed flows may either be laminar or transition to turbulent and the pulsatile character of the flow has a significant effect on this transition to turbulence, which represents an abnormal flow nature in the circulation, and the development of transition to turbulent flow in the arteries has clinical interest as outlined above. From the point of view of accurate computational modelling, such flow can be challenging because the obstruction presented by a moderate or severe arterial stenosis can lead to a highly disturbed flow region downstream from the stenosis.

Numerous experimental studies for steady turbulent flow in arteries or tubes have been carried out by Giddens and his co-workers, for example, see Despande and Giddens [3] where the turbulent flow of water in a constricted tube was investigated by the Laser-Doppler Anemometer method with the Reynolds number (Re) ranging from 5000 to 15000. However, this range of Reynolds number is unrealistic for representing blood flow in arteries, as the typical range of Re of blood flow in human blood vessels varies from 1 in small arteries to approximately 4000 in largest artery (the aorta), Ku [4]. In the further studies of Khalifa and Giddens [5] and Ahmed and Giddens [6], although a moderate Reynolds number was used in the experiment, these are limited to steady turbulent flow. To date, to the authors' knowledge, there appear to have a very few experimental study on the pulsatile post-stenotic flow, notably Ahmed and Giddens [7] and Lieber and Giddens [8].

The fluid dynamics of post-stenotic blood flow plays an important role in diagnosis of arterial disease, for example the quantification of arterial stenosis by both duplex ultrasound and quantitative flow MRI techniques relies on measurements of the flow velocity/acceleration at/beyond the stenotic segment to infer the degree of underlying stenosis. Computational modelling has been used for the analysis of these flows, see Tutty [9], Tu *et al*. [10], Lee *et al.* [11] and Deplaon and Siouffi [12]. However, most computational studies focused on only 2D laminar flows as a 3D computational modelling of such flows in the transitional and turbulent region is quite challenging. In the context of 3D computation some recent works are cited here, see Mallinger and Drikakis [13], Sherwin and Blackburn [14] who used additive pulsation in their models. Very recently Varghses *et al.* [15; 16] have investigated the steady and pulsatile flow in symmetric and eccentric stenoses and reported the results of the turbulence phenomena at the downstream of the eccentric stenosis for relatively low Reynolds numbers.

In addition to those, some axisymmetric computational investigations for laminar to turbulent flow have been studied by Ghalichi *et al.*[17], Lee *et al.* [18; 19] by using the Reynolds-average Navier-Stokes (RANS), particularly, the k-ω turbulence model. But Scotti and Piomelli [20] clearly indicated the limitations of using the conventional RANS turbulent models to study pulsatile flows. These models are incapable of predicting the time accurate flow as the governing equations of motion are time-averaged. The Large Eddy Simulation (LES) approach, which somewhat lies between Direct Numerical Simulation (DNS) and RANS, has already proved to be an excellent technique for modelling a turbulent flow. In DNS, where all the large and small scales are resolved, but in LES, only the large scales, that means, the energy-containing scales of turbulence are resolved while the smaller (subgrid) scales (SGS) are modelled. DNS is suitable for a low Reynolds number flow but LES is applicable for a small to high Reynolds number flow and requires less time and mesh than DNS, since in LES only the smallest scales need not to be resolved.

So, the general aim of this paper is to perform the Large Eddy Simulation to study the post-stenotic phenomena of pulsatile flow through a simple biological type arterial stenosis by applying two different types of pulsation which are termed here as "additive" and "non-additive" as in Loudon and Tordesillas [21]. In the additive pulsation, the streamwise mean velocity is simply added with the unsteady sine pulse for which the volumetric flow rate never gets zero. While in the case of non-additive pulsation, the streamwise velocity varies with time in a way that the volumetric flow rate becomes zero at the start and end of every cycle (Tutty [9]). As it was argued by Pedley [22] that a highly pulsatile flow is not believed to be additive, i.e. non-additive or oscillatory, therefore, particular focuses are given in the paper on the investigation of non-additive pulsatile flow. In addition, some comparisons of the non-additive pulsatile results are given with those of the additive pulsatile and steady flows. We note that the most previous applications of LES are largely found in other engineering contexts, apart from the most recent works of Paul *et al.* [23] and Molla *et al.* [24] who investigated the pulsatile turbulent blood flow through the same model of arterial stenosis applying the LES technique for the Reynolds number of 1200. In addition to these two papers, Mittal *et al.* [25] investigated the pulsatile flow in a planar channel with a semi-circular type constriction or stenosis

by LES using an additive pulse.

2 Formulation of the problem

The geometry shown in Fig. 1 consists of a 3D channel with a one-sided cosine shape stenosis on the upper wall centred at $y/L = 0.0$ where y is the horizontal distance or the distance along flow and L is the height of the channel. In the model the height (x) and its width (z) are kept the same which forms a square cross-section at both upstream and downstream of the stenosis. The length of the stenosis is equal to twice that of the channel height, the stenosis reduces the channel cross-sectional area of 50% and its formation in the model is eccentric which is created using

$$\frac{x}{L} = 1 - \delta_c \left(1 + \cos\frac{y\pi}{L}\right), \quad -L \leq y \leq L, \tag{1}$$

where δ_c is the parameter related to the percentage of stenosis. Note that this formulation provides a smooth constriction whose geometry is reasonable representation of a biological type arterial stenosis, see [3].

From Pedley [26] and Fung [27], it is known that the blood flow in a large vessel can be modelled accurately as a Newtonian fluid, which refers to use the Navier-Stokes equations of motion for investigating the post-stenotic flow physics of blood through the model of the arterial stenosis considered in the paper. After applying a spatial filter (top-hat) to the system of governing equations, we achieve

$$\frac{\partial \bar{u_j}}{\partial x_j} = 0, \tag{2}$$

$$\frac{\partial \bar{u_j}}{\partial t} + \frac{\partial \bar{u_i}\bar{u_j}}{\partial x_j} = -\frac{1}{\rho}\frac{\partial \bar{P}}{\partial x_i} + \frac{\partial}{\partial x_j}\left[\nu\left(\frac{\partial \bar{u_i}}{\partial x_j} + \frac{\partial \bar{u_j}}{\partial x_i}\right)\right] - \frac{\partial \tau_{ij}}{\partial x_j}, \tag{3}$$

where bar indicates the filtered variable, P is the pressure, t is the time, ρ is the fluid density, ν is the kinematics viscosity, and $u_j = (u, v, w)$ are the velocity vectors along the coordinate system, $x_j = (x, y, z)$, respectively. The effects of the small scales that appear in the subgrid-scale stress term as $\tau_{ij} = \overline{u_i u_j} - \bar{u_i}\bar{u_j}$ are modelled by employing the Smagorinsky model [28],

$$\tau_{ij} - \frac{1}{3}\delta_{ij}\tau_{kk} = -2\nu_{sgs}\bar{S}_{ij} = -2(C_s\triangle)^2|\bar{S}|\bar{S}_{ij}, \tag{4}$$

where C_s is the Smagorinsky constant obtained via the dynamic subgrid model of Germano-Lilly [29; 30] clipping the negative values of the constant C_s to zero; $\triangle = \sqrt[3]{\triangle x \triangle y \triangle z}$ is the filter width; and $|\bar{S}| = \sqrt{2\bar{S}_{ij}\bar{S}_{ij}}$ is the magnitude of the large scale strain rate tensor, $\bar{S}$.

2.1 Boundary conditions

In the case of simple steady inflow profile, the fully developed streamwise velocity which is imposed at the inlet of the channel is derived as

$$\bar{v}(x) = 6\bar{V}\frac{x}{L}\left(1 - \frac{x}{L}\right), \tag{5}$$

where $\bar{V}$ is the average streamwise velocity.

To generate the additive pulsatile velocity profile at the inlet, the above parabolic inflow is varied with time in a way that the volumetric flow rate per unit channel width, L, varies according to

$$Q(t) = Q_{max}\Big[1 + a_m \sin\Big(\frac{2\pi t}{T}\Big)\Big], \tag{6}$$

where T and a_m are the time period and the amplitude of the pulsation, respectively. Therefore, the streamwise velocity for the additive pulsation can now be derived as,

$$\bar{v}(x,t) = 6\bar{V}(t)\frac{x}{L}\Big(1 - \frac{x}{L}\Big) = 6\bar{V}_{max}\frac{x}{L}\Big(1 - \frac{x}{L}\Big)\Big[1 + a_m \sin\Big(\frac{2\pi t}{T}\Big)\Big], \tag{7}$$

where $\bar{V}_{max}$ is the velocity at the maximum flow rate of Q_{max} and the Reynolds number at this peak flow rate is now defined as $Re = \bar{V}_{max}L/\nu$. It is clear from the above relations (6-7) that the volumetric flow rate with the additive pulsatile profile never gets zero at any position of time when $a_m \neq \pm 1$. Note that the similar velocity profile was used by Lee *et al.* [11] to investigate the effects of additive pulsatile amplitude on the unsteady laminar flow in a pipe with ring-type stenosis or constriction.

In the non-additive pulsatile case, the parabolic inflow shown in Eq. (5) varies in a manner similar to Tutty [9], where the volumetric flow rate, $Q(t)$, per unit channel width, L, is varied in a sinusoidal manner with time as

$$Q(t) = \frac{Q_{max}}{2}\Big[1 - \cos\Big(\frac{2\pi t}{T}\Big)\Big], \tag{8}$$

so that the flow rate at the start and end of every pulsation becomes zero and the maximum at the mid-location of every pulse. Finally, the streamwise velocity profile for the non-additive pulsation is formulated as

$$\bar{v}(x,t) = 6\bar{V}(t)\frac{x}{L}\Big(1 - \frac{x}{L}\Big) = 3\bar{V}_{max}\frac{x}{L}\Big(1 - \frac{x}{L}\Big)\Big[1 - \cos\Big(\frac{2\pi t}{T}\Big)\Big]. \tag{9}$$

In Fig. 2 the the volumetric flow rate, $Q(t)/Q_{max}$, for the additive and non-additive pulsatile profiles are illustrated graphically for one-cycle to show clearly the variation of the flow rates between the two pulses. In the figure we have used $a_m = 1$ for the amplitude of the additive sine pulse. The peak-to-mean ratio for the non-additive pulsatile profile is 0.5, while the ratio varies for the additive pulse with its amplitude, a_m.

No slip boundary conditions are used for both the lower and upper walls of the model, and at the outlet a convective boundary condition is applied which is as,

$$\frac{\partial \bar{u}_i}{\partial t} + U\frac{\partial \bar{u}_i}{\partial y} = 0, \tag{10}$$

where U is the convection velocity which takes the constant mean exit velocity. In the spanwise boundaries, a periodic boundary condition is applied to model the spanwise homogeneous flow. Non-uniform dense meshes are used near both the

top and bottom walls of the model to capture the thin shear layer developed in the vicinity of the walls. In addition, the meshes are concentrated at the region immediate downstream of the stenosis where the flow separation takes place.

The governing filtered equations (2-3) subject to the above boundary conditions are solved using an in-house developed LES code which is second order accurate in both time and space and fully implicit, for details about the numerical algorithm see Jones and Wille [31]. The average time step, dt, the computation used is at the order of 10^{-3}, which ensures that the maximum Courant number always lies between 0.1 and 0.2. The simulations are carried out up to the total of ten cycles of pulsation, where the mean flow eventually reaches a stationary state.

3 Results with discussion

3.1 Validation with experiment

In this section, a comparison of the present computational results is made with those of the experimental investigation of the post-stenosis flow performed by Ahmed and Giddens [6]. An axisymmetric model of the stenosis is considered here for making this comparison with an area reduction of 50% at the centre of the stenosis, and the flow Reynolds number in the simulation is fixed at 1000 as was done by [6]. The boundary condition in the inlet is treated as a fully developed laminar pipe flow without adding any pulsation to this, while the lower wall of the model shown in Fig. 1 is treated as a symmetric plane. The governing flow field found in the downstream of the stenosis is laminar with a negligible effect coming from the SGS, which is essentially a DNS computation. The comparison, presented in Fig. 3 for the streamwise velocity at different downstream locations, shows clearly that the overall agreement of the present computational results against the experiment [6] is quite good indeed. At $y/L = 0.0$ and $y/L = 0.5$, the computational velocity profiles slightly deviate in the middle portion of the computational domain but have good agreement at the wall and centre.

3.2 Non-additive pulsatile results

3.2.1 Mesh independent test

In order to check what would be the appropriate grid density that is required for LES in the present model, we have chosen three different grid configurations, $50\times200\times50$, $50 \times 250 \times 50$ and $70 \times 250 \times 50$, for $Re = 2000$ imposing the non-additive pulsation (Eq. 9) in the inlet. The results of this mesh independent test are presented in Fig. 4 for the time mean streamwise velocity at four different axial positions (frames a, b) and for the mean kinetic energy (MKE) at the centre of the model (frame c). Note that the streamwise velocity results in frames (a)-(b) have been normalised by the average velocity.

As can be seen in this figure that the comparison of the above mean results between the three-grid setup agree quite well with each other, which clearly indicates that the flow resolution is not remarkably sensitive with these grid orientations. In

addition, a comparison of the turbulent kinetic energy (TKE) is presented in § 3.2.4 where a satisfactory agreement is obtained. Therefore, based on this agreement and to minimise the computational space and time, the $50 \times 200 \times 50$ grid setup is assumed to be sufficient for the LES at $Re = 2000$. The same grid is followed through the computations of both additive and non-additive pulsations for the other Reynolds numbers less than 2000.

Fig. 4 shows that the mean velocity near the inlet, at (i) $y/L = -0.2$, has a parabolic shape, as expected, because of the laminar nature of the flow at the upstream. However, it is deformed at the centre of the stenosis, at (ii) $y/L = 0.0$, with the peak becoming approximately double in magnitude and where the flow separation starts to take place. At the post stenosis regime this parabolic shape breaks down and the separated flow now takes an anomalous form as shown in frame (b). At (iii) $y/L = 1.0$, there is a further increase in the magnitude of the velocity, as a result the MKE gets its maximum value around this location. The negative velocity found in (iii)-(iv) near the upper wall is caused by the adverse pressure gradient.

3.2.2 SGS contribution

In Figs. 5 and 6 the contribution of the SGS model obtained by the non-additive pulsation is illustrated. The results of the dynamic Smagorinsky constant, C_s, for $Re = 1700$ and 2000 are presented in Fig. 5, while the corresponding SGS eddy viscosities, μ_{sgs}, which have been normalised by the molecular viscosity, μ, are presented in Fig. 6. The contour levels in Fig. 5 show clearly that the value of C_s is significantly high at the downstream of the stenosis because of the nature of the flow which is turbulent (see § 3.2.4). In addition, C_s attains a maximum value of about 0.105 for $Re = 2000$, which is very close to 0.1 – a typical value of the Smagorinsky constant usually used for LES of turbulent flow in a channel. The maximum eddy viscosity for this case is found about 0.78, which corresponds to the fact that the SGS model contributes up to a maximum of 78% extra dissipation into the flow. While for $Re = 1700$ it is about 27%, which is reasonable, because for the lower Reynolds number the energy reduces in the SGS flow. This maximum SGS dissipation takes place at the post stenosis region, whereas no dissipation is seen in the region before the stenosis as the flow remains laminar there. Also note that the contribution of SGS model found for $Re = 1500$ is very small, indicating the fact that the DNS rather than LES would be preferable for simulation of $Re \leq 1500$.

3.2.3 Instant flow field

To represent the instant flow field downstream of the stenosis, the $\bar{u} - \bar{w}$ velocity components are presented in Fig. 7 at different cross-sectional positions of the post stenosis region, which are obtained by the non-additive pulsation imposed at the inlet while $Re = 2000$. Although, by inspecting these vector plots, an immediate conclusion can be drawn on the nature of the flow found at the downstream of the stenosis, which is fully three-dimensional and turbulent; some detailed assessments of this transient flow will follow in the subsequent sections, as our main intention

here is to provide some qualitative assessments on the flow field downstream of the stenosis.

It can be seen in (a) $y/L = 0$, which is the location of the throat of the stenosis, that the flow phenomenon is clearly transitional with some vortical structures beginning to form in the flow located at the central region. The intensity of these vortices grows rapidly towards the immediate downstream of the stenosis, at (b)-(d), which could have some dramatic impacts in terms of causing blood-clot and generating turbulent fluctuations in the post-stenotic flow, which will be discussed in more details latter. However, towards the further downstream, at (e)-(f), the vortex intensities gradually decrease as the effect of the stenosis on the flow reduces there.

In Fig. 7 the cross-sectional flow has been presented, while for illustrating the flow in the streamwise direction the results of the spanwise-averaged vorticity (ω_z) are presented in Fig. 8 as contours for different Reynolds numbers, (a) $Re = 1000$, (b) $Re = 1200$, (c) $Re = 1500$, (d) $Re = 1700$ and (e) $Re = 2000$. Note that in each frame, a total of 14 unequal contour levels are plotted between their maximum and minimum values which can easily be seen in the colour bar. In addition, the dashed contour lines correspond to the negative values of ω_z where the vortex cells rotate in the anti-clockwise direction, while the solid lines are for representing the positive contours where the vortex rotates in the clockwise direction. It can be seen that for all the Re cases one clockwise and another anti-clockwise vortices are developed at the post-lip of the stenosis, clearly seen in the first four frames. These phenomena can be attributed by the fact that the shear layer which is generated by the increasing velocity in the centre of the stenosis (Fig. 4a) separates from the nose and rolls as an anti-clockwise rotating vortex in the post-lip region of the stenosis, whilst the second shear layer separating from the opposite surface of the nose induces a clockwise vortex near the lower wall. Moreover, the contour levels indicate that the strength of these pair vortices increases with the Reynolds number, and the post stenotic flow structure for $Re = 2000$ is quite sensitive and turbulent, see in frame (e), where the pair vortices break down, as a result the flow pattern becomes very complex and random, which in turn, causing oscillations in the pressure and shear stress distributions at the post stenosis region (presented latter in Figs. 21 and 22).

The spanwise-average vorticity at the different phases of the last time cycle are plotted in Fig. 9 for $Re = 2000$. Through all the frames, the development of the flow transition to turbulent downstream of the stenosis may be observed. In frame (a), the primary shear layer developed in the region from $y/L \sim 0.7$ to $y/L \sim 1.5$ breaks down into vortices, while the secondary shear layer which lies between $y/L \sim 1.7$ and $y/L \sim 2.0$ generates the clockwise vortices that roll down to the downstream with time as shown in frames (b)-(f). The intensity of these vortices decreases towards the further downstream region. After phase $t/T = 9.5$ i.e. after the peak position of the flow, frames (g)-(j) show the further development of the two shear layers from the centre of the stenosis and at the end of cycle they are gradually taking the stance which were seen in frame (a).

3.2.4 Turbulent characteristics

In this section some results of the turbulent flow quantities will be summarised. In this regard, the results of the centreline turbulent kinetic energy, $TKE = \frac{1}{2} < u_j'' u_j'' >$, for the non-additive pulsation are presented in Fig. 10 for the three different Reynolds numbers, 1500, 1700 and 2000. The results presented with the symbol lines for $Re = 2000$ have been obtained by using the two higher grid resolutions such as $50 \times 250 \times 50$ and $70 \times 250 \times 50$, see § 3.2.1 for details. Note that the TKE results have been normalised by $\bar{V}_{max}^2$ where $\bar{V}_{max}$ corresponds to the bulk velocity taken from $Re = 2000$.

Before the centre of the stenosis the turbulent kinetic energy for all the three Re cases becomes approximately zero because of the laminar nature of the flow at the upstream of the stenosis, but the intensities of TKE grow substantially towards the immediate downstream of the stenosis though they depend on the Reynolds number. The extreme level of TKE is recorded at the region of $1 \leq y/L \leq 4$ for all cases, and the intensities of the turbulent kinetic energy reduce gradually after $y/L \sim 6$ and they approach to zero to the far downstream region where the effect of stenosis vanishes.

To give more clear evidence on the presence of the turbulent flow downstream of the stenosis, the energy spectra of the streamwise velocity fluctuations, $v''^2/\bar{V}_{max}^2$, and the pressure fluctuations, $p''^2/(\rho\bar{V}_{max}^2)^2$, are presented in Figs. 11 and 12, respectively, against the Strouhal number, $Sr = (fL/\bar{V}_{max})$, of the vortex shedding frequency, f. For these energy spectra the fluctuating results have been obtained by the non-additive pulsation for $Re = 2000$ at four different downstream positions, (i) $y/L = 1.0$, (ii) $y/L = 2.0$, (iii) $y/L = 3.0$, and (iv) $y/L = 4.0$. The lines corresponding to $(Sr)^{-5/3}$ are included in the figures to show clearly the broadband frequency regions or inertia sub-range frequency regions of the turbulent flow achieved in the post stenosis. Also it should be mentioned here that the energy spectra were tested at the far downstream region and a very much shorter inertia sub-range region was found compared to what is seen in Figs. 11 and 12, which is again proving the fact that the turbulent intensity is negligible at the far downstream.

3.3 Additive vs. non-additive pulsations

In this section the development and structure of the transient flow found at the downstream of the stenosis for the non-additive pulsations will be compared with those of the additive pulsatile and steady flows. With this in mind, some additional computations have been performed here applying (i) a simple fully developed steady flow at the inlet and (ii) an additive type pulsation where the mean/steady flow profile is added with a sine pulse, the details of the inlet velocity profiles have been given in § 2.1. The results of the instant spanwise-average vortices, wall shear stresses and the mean streamlines will be compared in § 3.3.1, while some direct comparisons of the mean velocity, pressure and shear stresses between the non-additive and additive cases will be presented in § 3.3.2.

3.3.1 Comparisons of the instant and mean flow fields

The spanwise vortices are presented in Fig. 13 for (a) $Re = 1000$ and (b) $Re = 1200$ which are obtained by imposing the fully developed steady streamwise velocity in the inlet of the model. In this case, the flow structures found at the downstream of the stenosis are quite different compared to what were observed in Fig. 8. In addition, as reported by Pedley [22], this 2D Poiseuille type flow can not be found anywhere in human blood vessel because blood vessels are typically short, curved, branched and elastic and the flow through a blood vessel is unsteady. Therefore, a sinusoidal pulsation adding to this steady/mean flow may misinterpret the transient flow downstream of a stenosis. To clarify this fact fully the spanwise vortices obtained by the additive pulsation are depicted in Fig. 14. Note that the amplitude of the additive pulsation is taken as $a_m = 0.1$ for Fig. 14(a)-(b) and 0.2 for Fig. 14(c). When $a_m = 0.1$, the peak Reynolds number of the flow attains at 1100 for $Re = 1000$, while it is 1320 for $Re = 1200$. In both cases the large vortices at the post-stenosis dominate the flow and roll down to the downstream. On the other hand, when $a_m = 0.2$ the peak Reynolds number becomes 1440 for $Re = 1200$, the vortex rolling in the post stenosis region persists but the intensity of the turbulent grows. Again, as it can clearly be seen in Fig. 14 that the additive pulsations produce the flow at the downstream of the stenosis whose structures are quite different than those of the non-additive pulsations (Fig. 8).

In Fig. 15 the instantaneous upper wall shear stresses between the non-additive and additive pulsatile are compared at the different phases of the last time period while $Re = 1200$. Here a 10% sinusoidal oscillation is added in the additive pulsatile case. In frame (a), at the initial phase of the 9th cycle of the time period, the shear stress drops at the throat of the stenosis and the oscillatory nature of the shear stress at the post stenotic region is found higher for the additive case than the case of non-additive. Though the shear stress for the non-additive case in frame (b), at $t/T = 9.1$, is almost same as in frame (a), the stress drop as well as oscillation in stress for the additive case increases in the post stenotic region. However, towards the further downstream region, the shear stresses are smaller in the additive case than the non-additive pulse.

Near the peak phase of the additive case (at $t/T = 9.2$) the shear stress drop achieves its extreme magnitude of -0.07487 at $y/L = -0.091$, while the corresponding stress drop in the non-additive case is -0.01809 located at $y/L = 0.0$. The stress drop in the additive case decreases at $t/T = 9.3$, but it increases in the non-additive case and gives a maximum at the location of its peak phase (frame (f)). The magnitude of this maximum is about -0.04227 occurring at $y/L = -0.091$. After this phase, the pattern of the shear stresses gradually approaches to that observed in frame (a).

The corresponding lower wall shear stresses are presented in Fig. 16(a-i). The oscillating nature in the shear stresses is also present in the lower wall and the intensity of that is again higher for the case of additive than non-additive. The maximum shear stress found for the additive case occurs at the lower wall just opposite to the throat of the stenotic region, while for the non-additive case the position of the maximum shear stress at some phases moves slightly to the downstream.

Significant variations are also clearly evident in the mean streamline profiles pre-

sented in Figs. 17 to 19 for the non-additive pulsatile, steady and additive pulsatile flows, respectively. In addition, the strength of the recirculation at the post-stenosis is found much higher for the additive pulsations than the non-additive cases. In the pathological context, this flow recirculation usually increases the staying time of blood at the downstream region of the stenosis that may cause heart attack or brain stroke as the flow at each cycle is reversed there for a significant time. Furthermore, these are the regions for low and adverse pressure gradient of the flow.

3.3.2 Some direct comparisons of the mean results

In this section some additional physics of the mean flow at the post-stenosis will be revealed through the results of the velocity, pressure and shear stresses, which are presented in Figs. 20 to 22, respectively. In addition, some direct comparisons between the non-additive and the additive pulsatile results will be made here for $Re = 1000$ and 1200. The mean results of the non-additive pulsation for different Reynolds numbers are depicted in Figs. 20-22 using the lines without any symbols, while the solid lines with symbols represent the additive pulsatile results.

Fig. 20 shows that the peaks of the mean centreline velocity for the additive pulsations occur just after the centre of the stenosis located at about $y/L = 0.2$ where the flow separation took place, already observed before. These centreline velocities then drop abruptly at the position close to the post-lip of the stenosis but attain their second peaks towards the further downstream at the position which is close to the reattachment of the large recirculation seen in Fig. 18. Comparing these with the non-additive pulsatile cases, the first peaks which occur at close to the centre of the stenosis create the second peaks near the post-lip of the stenosis after the initial drop. Moreover, the second peaks for the higher Reynolds numbers, e.g. when $Re \geq 1500$, become stronger than the first peaks, which have contributed in producing oscillations in the velocity field at the further downstream. Also note that, as already shown in Fig. 2, the mean flow strength in the additive case for $Re = 1000$ is equivalent to $Re = 2000$ in the case of non-additive pulse.

The mean pressure distributions at the upper wall, centreline and lower wall of the stenosis are shown in Fig. 21(a)-(c), respectively. For the non-additive pulsations, the maximum pressure drop for the upper wall occurs at the centre of the stenosis, while for the centreline the extreme pressure drop takes place at the post-lip of the stenosis. In addition, the oscillations found in the pressure profiles, which are clearly seen for the higher Reynolds number cases, correspond to the oscillations in the velocity field observed in Fig. 20. Again, we can see here that the downstream mean pressure profiles for the additive pulsations are quite different compared to the non-additive pulsations.

In Fig. 22 the corresponding mean shear stresses are presented. In the upper wall, where the stenosis appeared, the mean shear stresses obtained by the non-additive pulsation reduce abruptly at the centre of the stenosis (where the pressure drop was maximum) and they go to a peak level at the post-lip of the stenosis. However, the shear stresses for the lower wall initially rise at the centre of the stenosis and their magnitudes drop towards the downstream. Moreover, the significant level of oscillations found in the shear stresses has a quite important issue in medical context as this usually influences to cause potential damage to the materials of blood cells

in the post-stenosis region and also to the inner surface of a blood vessel. For the additive pulsatile cases, the mean shear stresses found in the downstream of the stenosis differ significantly from those obtained by the non-additive pulsations.

4 Conclusion

Large Eddy Simulation with the dynamic sub-grid model has been performed to study transition of the additive and non-additive pulsatile flows in a 3D model of arterial stenosis. To the best of the authors' knowledge, to-date this is the first attempt which provides an in-depth investigation of transition to turbulent of both additive and non-additive pulsatile flows at the downstream of a model of biological type arterial stenosis by using the LES. We have reported that the sub-grid model has a remarkable contribution to the resolved scale when the flow Reynolds number, Re, is greater than 1500, which justifies the importance of using LES in the modelling of pulsatile/biological type flow. The results of the mesh independent test presented for both the mean and turbulent quantities for the case of $Re = 2000$ are quite satisfactory, and the validation of the present numerical results with those of Ahmed and Giddens [6] also agrees quite well.

The mean streamwise velocity for the non-additive pulsation became approximately double at the centre of the stenosis where the flow separation started to take place. At the post stenotic region the flow is observed turbulent with the broadband frequency region of slope $-\frac{5}{3}$, and the flow pattern downstream of the stenosis is found quite complex due to the interaction between the two shear layers separated from the two opposite walls at the centre of the stenosis. In addition, the vortex intensity, which is found quite high near the post-lip of the stenosis, could have some potential medical consequences, e.g. damaging of the materials of blood cells in the post-stenotic zone. Furthermore, the mean streamlines show that the primary recirculating region is situated at the immediate downstream region of the stenosis, where the adverse pressure gradient takes place, and it is at the throat of the stenosis that the centreline velocity is highest and hence we have found the maximum pressure drop at this site.

When Re is high enough, both the pressure and shearing stresses take on an oscillating form at the post stenotic region. The vortex intensity and shear stresses observed quite high at the post-lip of the stenosis due to the maximum pressure drop occurring at this region, where the fluid transit is slower, i.e. a prolonged staying time. This prolongation of staying time is potentially dangerous from the pathological point of view as this stagnation could be a factor in the genesis of thrombosis (blood clotting) in the post stenosis region. Similar physical phenomena were found in the previous experimental studies, e.g. see [6; 8] who took a tube type geometry with stenosis.

We have demonstrated in the paper that the physical natures of the flow-transition and the patterns of the flow-streamline found in the downstream of the stenosis for the non-additive pulsatile cases are quite distinctive compared with those of both the steady and additive pulsatile flow cases. Despite the simplicity in the model of arterial stenosis studied here, we believe that the simulated results presented in the paper would give better insight and in-depth knowledge to a pathologist or

medical surgeon on the important fluid dynamics aspects of transient blood flow that usually present in a real-life biological stenosis e.g. pathological atherosclerotic stenosis. Moreover, a real biological stenosis may not be always symmetric (Stroud *et al.* [32], Varghses *et al.* [15]), therefore, the LES results presented in the model of the non-uniform asymmetric stenosis formed eccentrically on the top wall of the channel would be useful to understand the blood flow transition and turbulence in a biologically real asymmetric arterial stenosis. A general extension of this study is to consider a more biological realistic model of artery and investigate the transition of the two types of pulsations with fluid-structure interaction.

Acknowledgements: The authors thank to the anonymous reviewers for their valuable comments and suggestions on the earlier version of this paper, which have served to improve the manuscript.

References

[1] A. M. Malek, S. L. Alper, S. Izumo, Hemodynamic shear stress and its role in atherosclerosis, J. American Medical Association (JAMA) 282 (1999) 2035–2042.

[2] A. Frydrychowicz, A. Harloff, B. Jung, M. Zaitsev, E. Weigang, T. A. Bley, M. Langer, J. Hennig, M. Markl, Time-resolved, 3-Dimensional Magnetic Resonance Flow Analysis at 3 T: Visualization of Normal and Pathological Aortic Vascular Hemodynamics, J. Comput. Assist Tomogr. 31(1) (2007) 9–15.

[3] M. D. Despande, D. P. Giddens, Turbulent measurement in a constricted tube, J. Fluid Mech. 97(1) (1980) 65–89.

[4] D. N. Ku, Blood flows in arteries, Annu. Rev. Fluid Mech. 29 (1997) 399–434.

[5] A. M. A. Khalifa, D. P. Giddens, Characterization and evolution of poststenotic flow disturbances, J. Biomech. 14(5) (1981) 279–296.

[6] S. A. Ahmed, D. P. Giddens, Velocity measurement in steady flow through axisymmetric stenosis at moderate Reynolds number, J. Biomech. 16(7) (1983) 505–516.

[7] S. A. Ahmed, D. P. Giddens, Pulsatile poststenotic flow studies with Laser Doppler Anemometer, J. Biomech. 17(9) (1984) 695–705.

[8] B. B. Lieber, D. P. Giddens, Post-stenotic core flow behaviour in pulsatile flow and its effects on wall shear stress, J. Biomech. 23(6) (1990) 597–605.

[9] O. R. Tutty, Pulsatile flow in a constricted channel, J. Biomech. Eng. 114 (1992) 50–54.

[10] C. Tu, M. Delville, L. Dheur, L. Vanderschuren, Finite element simulation of pulsatile flow through arterial stenosis, J. Biomech. 25 (1992) 1141–1152.

[11] T. S. Lee, T. W. NG, Z. D. Shi, Numerical study of effects of pulsatile amplitude on unsteady laminar lows in rigid pipe with ring-type constrictions, Int. J. Numer. Meth. Fluids 24 (1997) 275–290.

[12] V. Deplano, M. Siouffi, Experimental and numerical study of pulsatile flows through stenosis: Wall shear stress analysis, J. Biomech. 32 (1999) 1081–1090.

[13] F. Mallinger, D. Drikakis, Instability in three-dimensional, unsteady, stenotic flows, Int. J. Heat and Fluid Flow 23 (2002) 657–663.

[14] S. J. Sherwin, H. M. Blackburn, Three-dimensional instabilities and transition of steady and pulsatile flows in an axisymmetric stenotic tube, J. Fluid Mech. 533 (2005) 297–327.

[15] S. S. Varghese, S. H. Frankel, P. F. Fischer, Direct numerical simulation of stenotic flows. Part 1. Steady flow, J. Fluid Mechanics 582 (2007) 253–280.

[16] S. S. Varghese, S. H. Frankel, P. F. Fischer, Direct numerical simulation of stenotic flows. Part 2. Pulsatile flow, J. Fluid Mechanics 582 (2007) 281–318.

[17] F. Ghalichi, X. Deng, A. D. Champlain, Y. Douville, M. King, R. Guidoin, Low Reynolds number turbulence modeling of blood flow in arterial stenosis, Biorheology 35(4-5) (1998) 281–294.

[18] T. S. Lee, W. Liao, H. T. Low, Numerical simulation of turbulent flow through series stenoses, Int. J. Numer. Meth. Fluids 42 (2003) 717–740.

[19] T. S. Lee, W. Liao, H. T. Low, Numerical study of physiological turbulent flows through series arterial stenoses, Int. J. Numer. Meth. Fluids 46 (2004) 315–344.

[20] A. Scotti, U. Piomelli, Turbulence models in pulsating flows, AIAA Journal 40(3) (2002) 537–544.

[21] C. Loudon, A. Tordesillas, The use of the dimensionless Womersley number to characterize the unsteady nature of internal flow, J. theor. Biol. 191 (1998) 63–78.

[22] T. J. Pedley, High Reynolds number flow in tubes of complex geometry with application to wall shear stress in arteries, In:Biological Fluid Dynamics, Edited by Ellington C P and Pedley T J, Cambridge: The Company of Biologiests, Limited (1995) 219–241.

[23] M. C. Paul, M. M. Molla, G. Roditi, Large-eddy simulation of pulsatile blood flow, em Medical Engineering and Physics 31 (2009) 153–159.

[24] M. M. Molla, M. C. Paul, G. Roditi, Physiological flow in a model of arterial stenosis, J. Biomechanics 41(S1) (2008) S243.

[25] R. Mittal, S. P. Simmons, F. Najjar, Numerical study of pulsatile flow in a constricted channel, J. Fluid Mech. 485 (2003) 337–378.

[26] T. J. Pedley, The fluid mechanics of large blood vessels, Cambridge University Press, 1980.

[27] Y. C. Fung, Biomechanics: Circulation, 2nd edition, Springer,1997.

[28] J. Smagorinsky, General circulation experiment with the primitive equations. i. the basic experiment, Monthly Weather Rev. 91 (1963) 99–164.

[29] M. Germano, U. Piomelli, W. Cabot, A dynamic subgrid-scale eddy viscosity model, Phys. Fluids A 3(7) (1991) 1760–1765.

[30] D. K. Lilly, A proposed modification of the Germano subgrid-scale closure method, Phys. Fluids A. 4(3) (1992) 633–635.

[31] W. P. Jones, M. Wille, Large-eddy simulation of a plane jet in a cross-flow, Int. J. Heat and Fluid flow 17 (1996) 296–306.

[32] J. S. Stroud, S. A. Berger, D. Saloner, Infuence of stenosis morphology on fow through severely stenotic vessels: implications for plaque rupture, J. Biomechanics 33 (2000) 443–455.

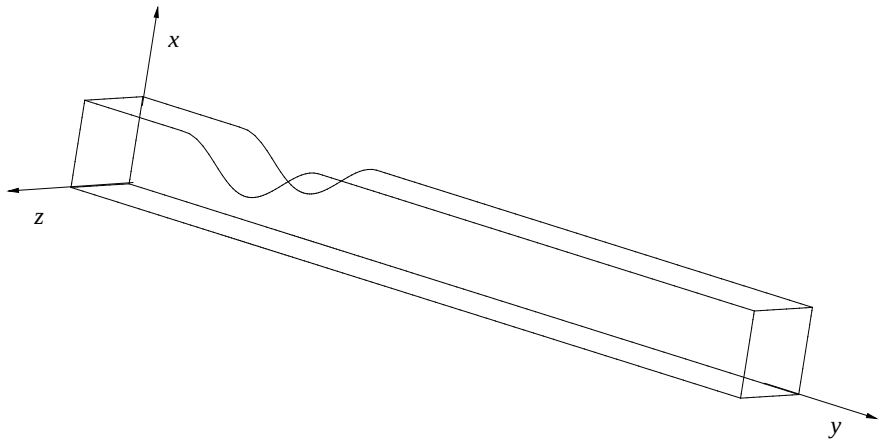

Figure 1: A schematic of the model showing the coordinate system.

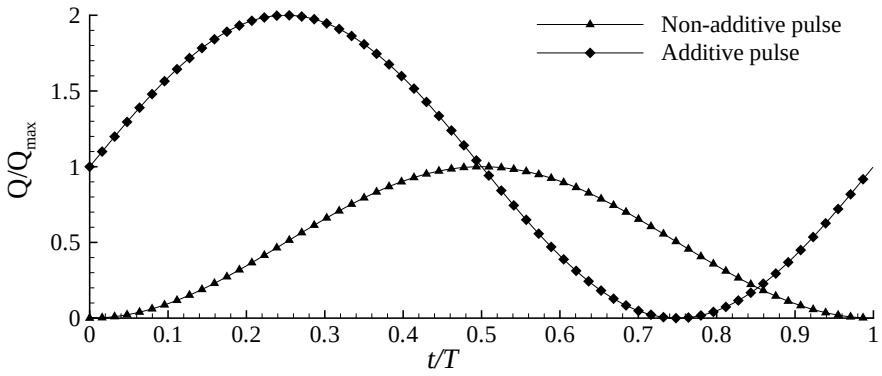

Figure 2: Difference between the non-additive and additive pulsatile volume flow rates.

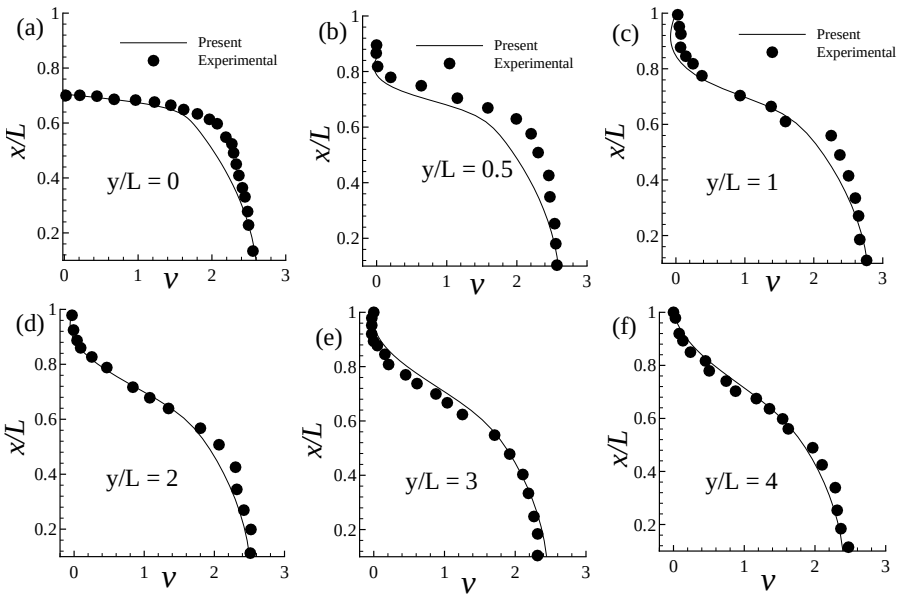

Figure 3: Comparison of $\bar{v}$ with the experimental results of [6] while $Re = 1000$.

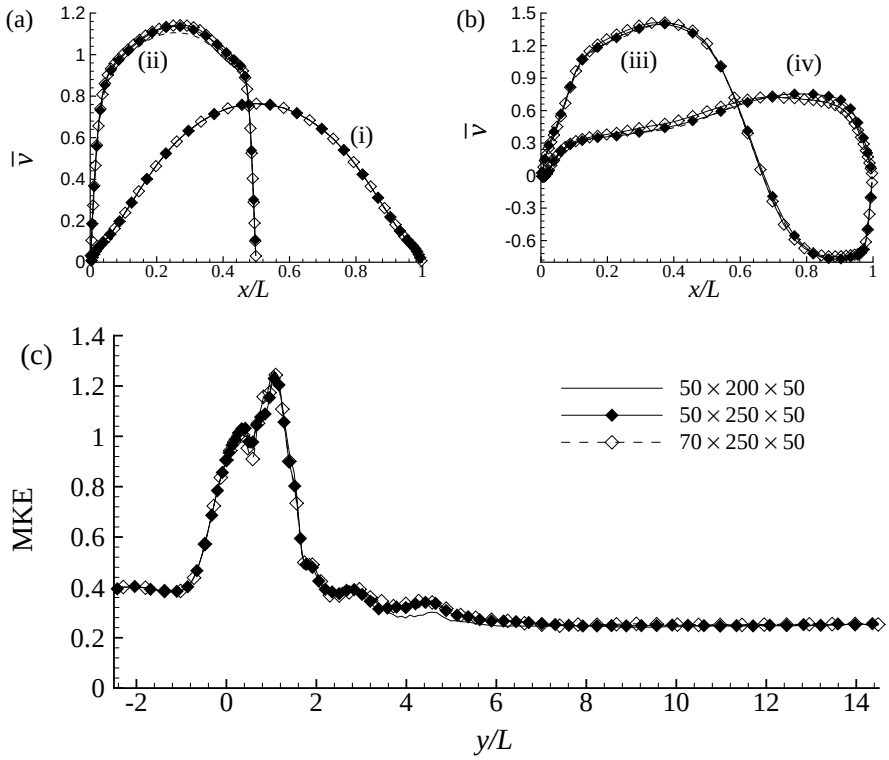

Figure 4: Normalised mean streamwise velocity (a-b) at (i) $y/L = -0.2$, (ii) $y/L = 0.0$, (iii) $y/L = 1.0$, and (iv) $y/L = 2.0$ and the centreline mean kinetic energy (c) obtained by the non-additive pulsation for $Re = 2000$.

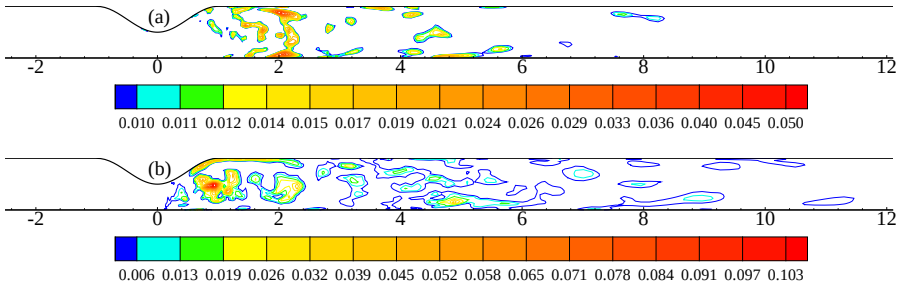

Figure 5: Dynamic Smagorinsky constant, C_s, at $t/T = 9.5$ obtained by the non-additive pulsation for (a) $Re = 1700$ and (b) $Re = 2000$.

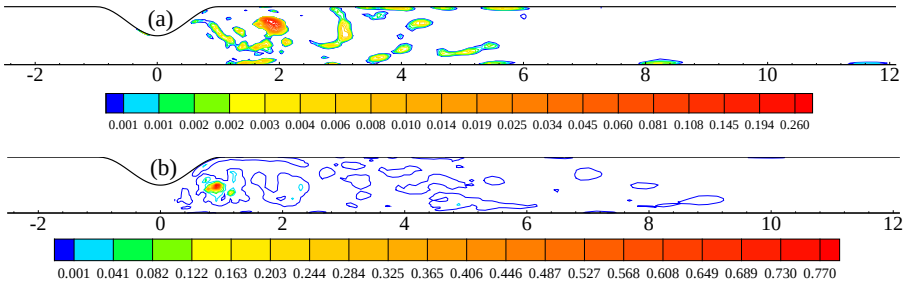

Figure 6: Normalised SGS eddy viscosity, μ_{sgs}/μ, at $t/T = 9.5$ obtained by the non-additive pulsation for (a) $Re = 1700$ and (b) $Re = 2000$.

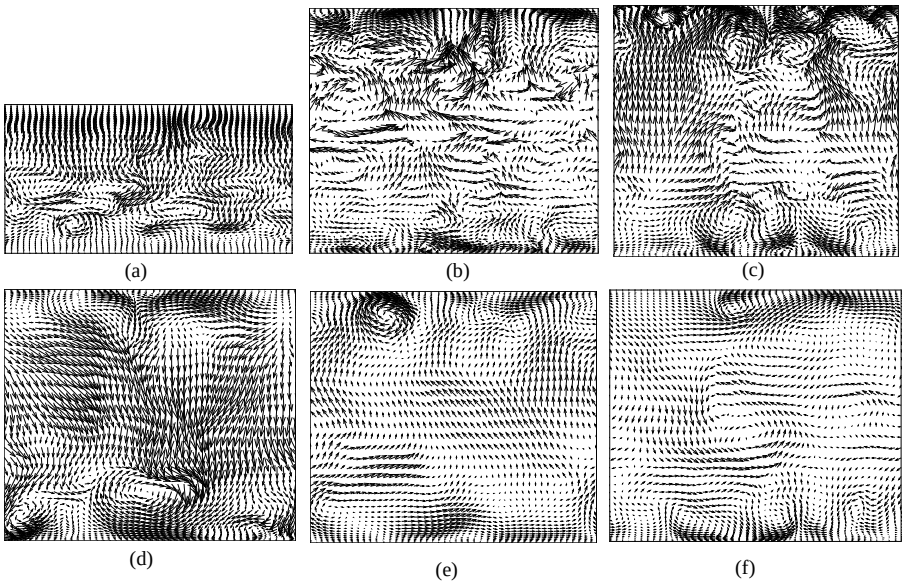

Figure 7: Instantaneous velocity vectors obtained by the non-additive pulsation at $t/T = 9.5$ for $Re = 2000$, here (a) $y/L = 0$, (b) $y/L = 1$, (c) $y/L = 2$, (d) $y/L = 3$, (e) $y/L = 4$, and (f) $y/L = 5$.

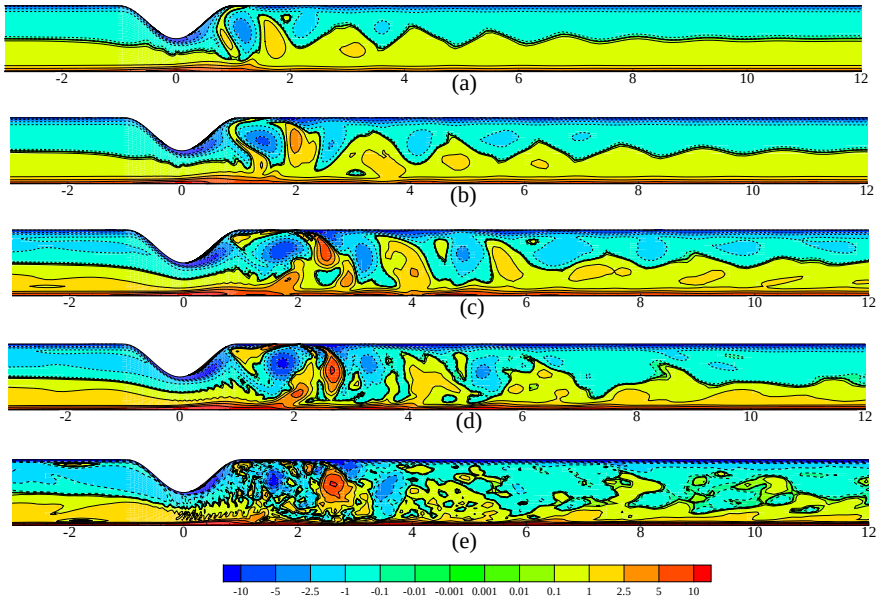

Figure 8: Spanwise average vorticity, ω_z, obtained by the non-additive pulsation at $t/T = 9.5$ for (a) $Re = 1000$, (b) $Re = 1200$, (c) $Re = 1500$, (d) $Re = 1700$ and (e) $Re = 2000$.

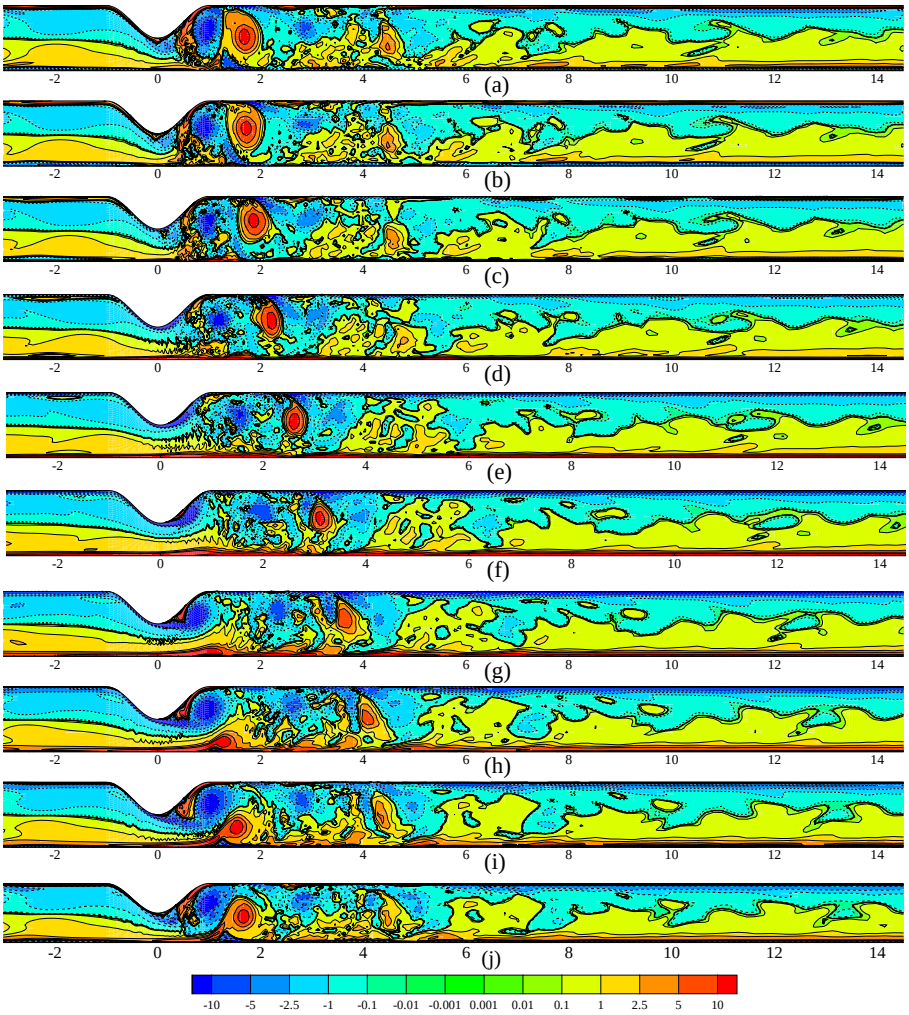

Figure 9: Spanwaise average vorticity, w_z, plotted at the different phases of time, (a) $t/T = 9.0$, (b) $t/T = 9.1$, (c) $t/T = 9.2$, (d) $t/T = 9.3$, (e) $t/T = 9.4$, (f) $t/T = 9.5$, (g) $t/T = 9.6$, (h) $t/T = 9.7$, (i) $t/T = 9.8$, (j) $t/T = 9.9$, while $Re = 2000$.

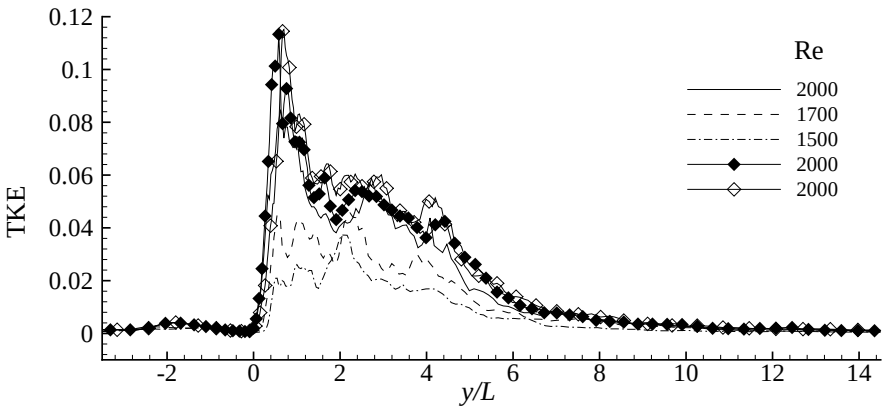

Figure 10: Centreline turbulent kinetic energy (TKE), $< u_j'' u_j'' > /2$, obtained by the non-additive pulsation for the three different Reynolds numbers.

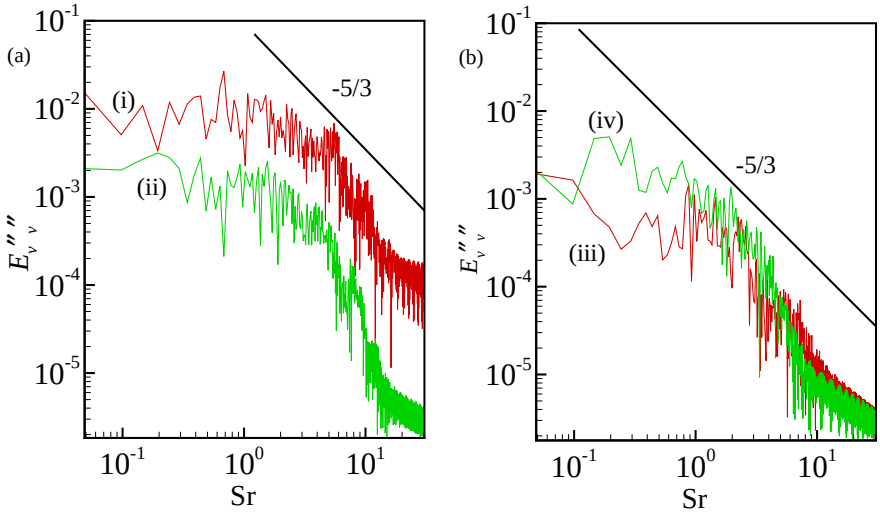

Figure 11: Energy spectra of v'' obtained by the non-additive pulsation for $Re = 2000$ at different downstream positions, (i) $y/L = 1.0$, (ii) $y/L = 2.0$, (iii) $y/L = 3.0$, and (iv) $y/L = 4.0$.

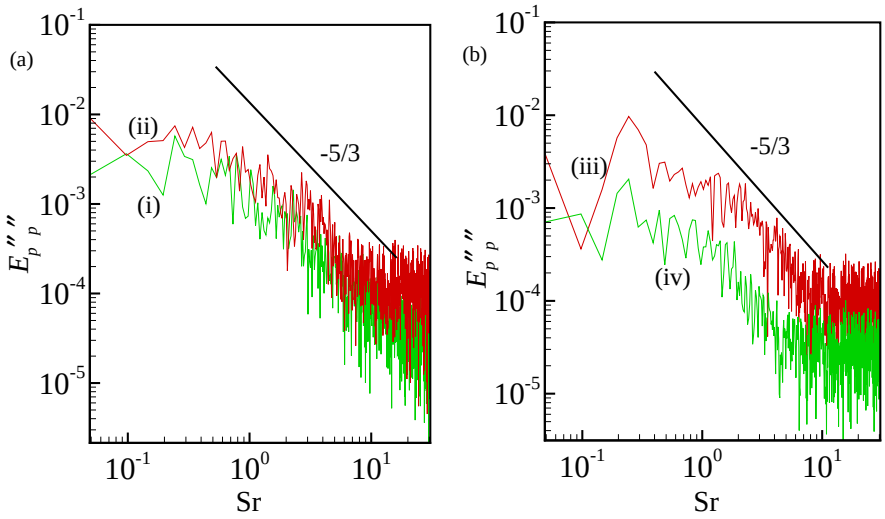

Figure 12: Energy spectra of p'' obtained by the non-additive pulsation for $Re = 2000$ at different downstream positions, (i) $y/L = 1.0$, (ii) $y/L = 2.0$, (iii) $y/L = 3.0$, and (iv) $y/L = 4.0$.

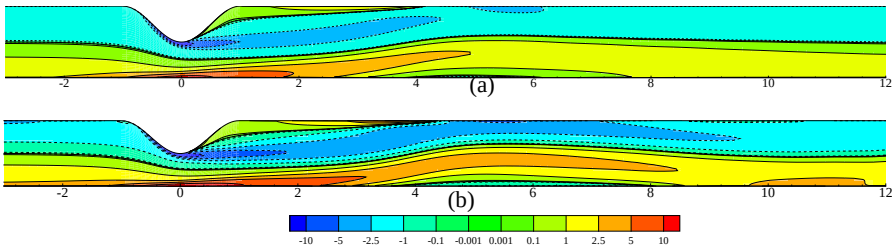

Figure 13: Spanwise average vorticity, ω_z, obtained by the steady inlet flow for (a) $Re = 1000$ and (b) $Re = 1200$.

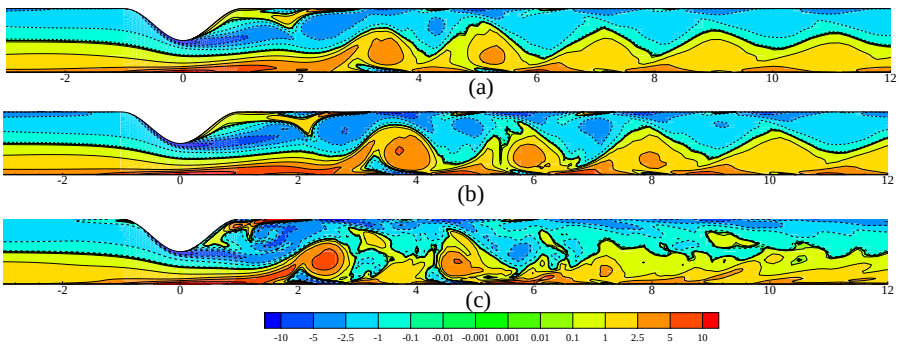

Figure 14: Spanwise average vorticity, ω_z, obtained with the 10% additive pulsation for (a) $Re = 1000$ and (b) $Re = 1200$, and the 20% additive pulsation for (c) $Re = 1200$.

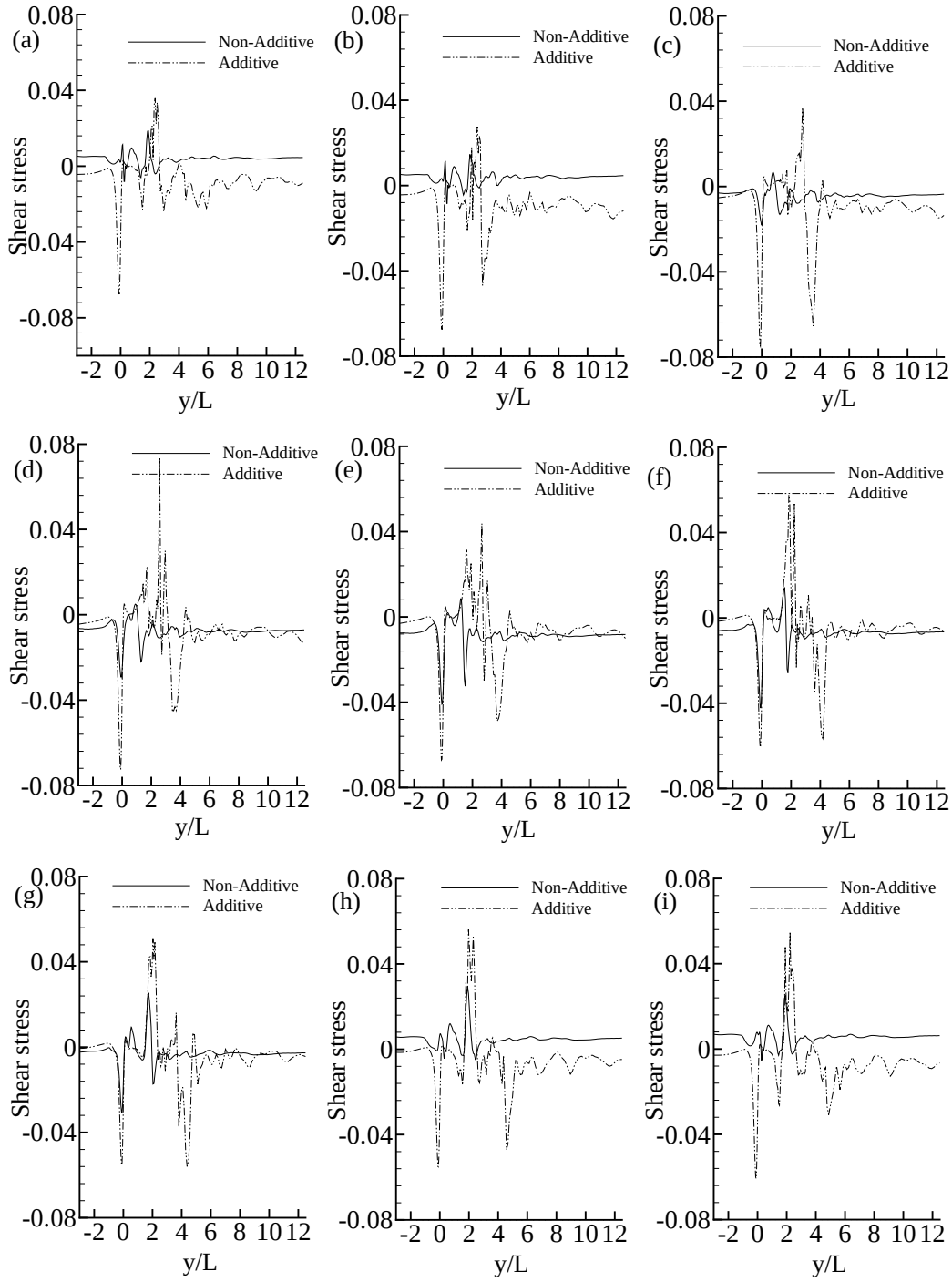

Figure 15: Instantaneous upper wall shear stress at the different phases of the last time period; (a) $t/T = 9.0$, (b) $t/T = 9.1$, (c) $t/T = 9.2$, (d) $t/T = 9.3$, (e) $t/T = 9.4$, (f) $t/T = 9.5$, (g) $t/T = 9.6$, (h) $t/T = 9.7$, (i) $t/T = 9.9$, while $Re = 1200$.

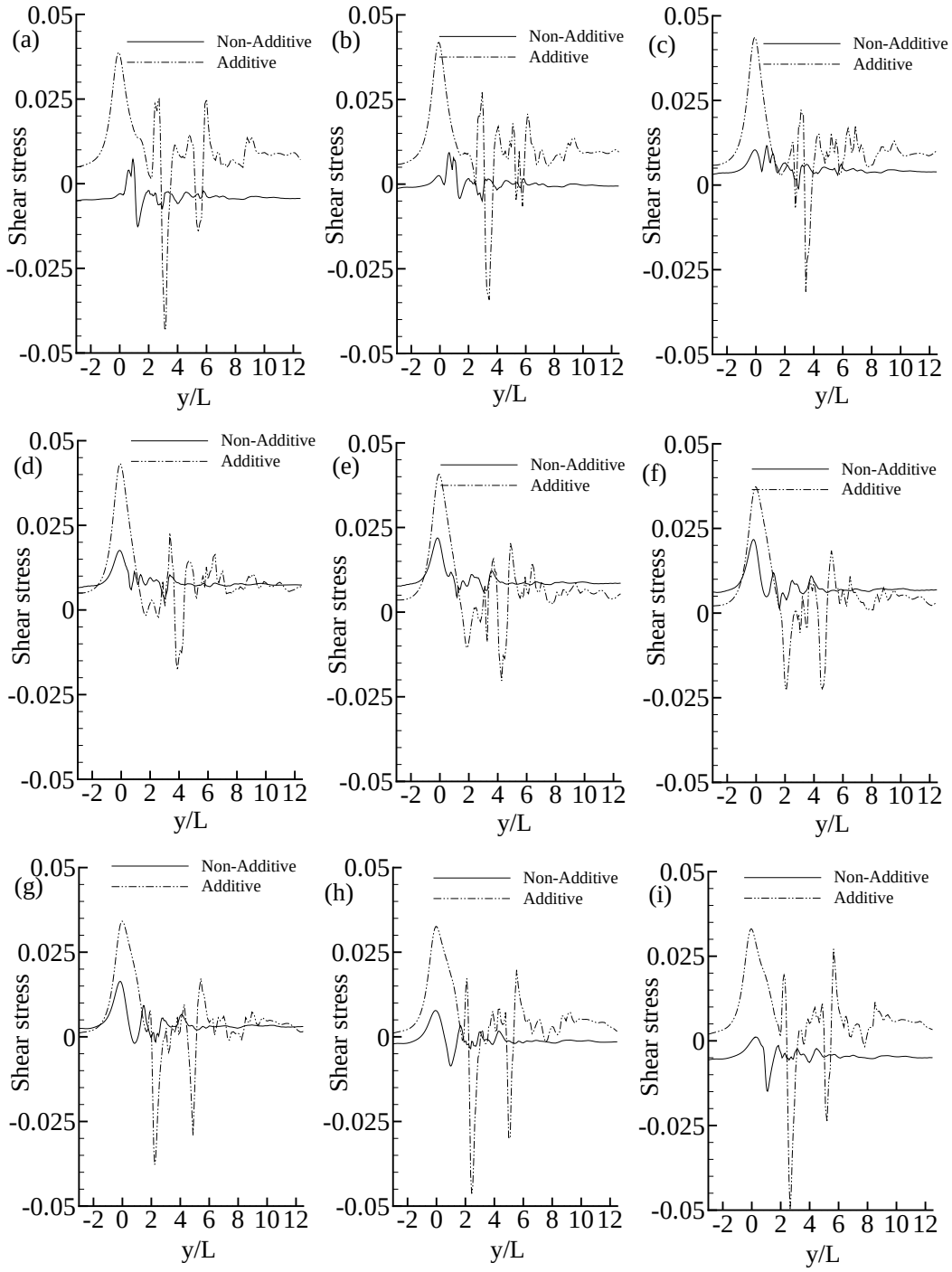

Figure 16: Instantaneous lower wall shear stress at the different phases of the last time period; (a) $t/T = 9.0$, (b) $t/T = 9.1$, (c) $t/T = 9.2$, (d) $t/T = 9.3$, (e) $t/T = 9.4$, (f) $t/T = 9.5$, (g) $t/T = 9.6$, (h) $t/T = 9.7$, (i) $t/T = 9.9$, while $Re = 1200$.

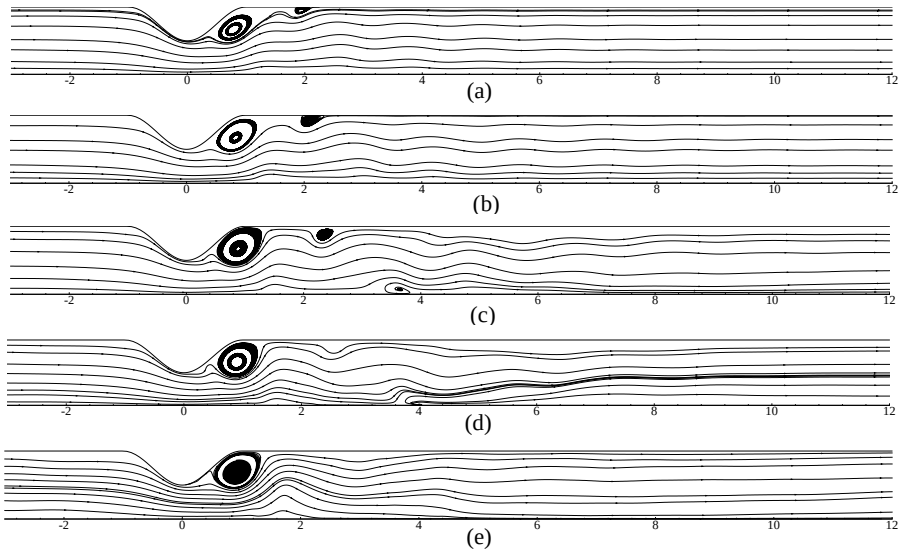

Figure 17: Mean streamlines obtained by the non-additive pulsation for (a) $Re = 1000$, (b) $Re = 1200$, (c) $Re = 1500$, (d) $Re = 1700$ and (e) $Re = 2000$.

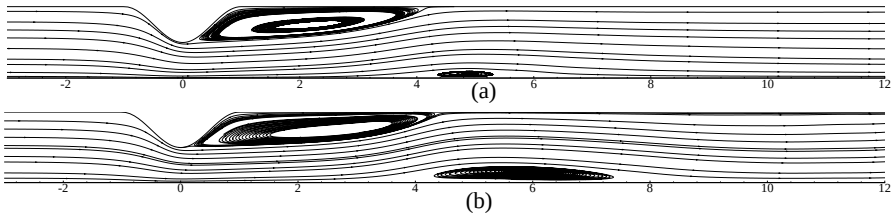

Figure 18: Streamlines obtained by the steady inlet flow for (a) $Re = 1000$ and (b) $Re = 1200$.

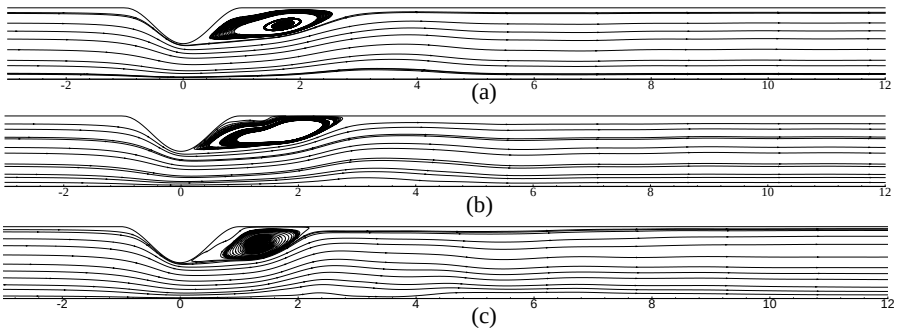

Figure 19: Mean streamlines obtained with the 10% additive pulsation for (a) $Re = 1000$ and (b) $Re = 1200$, and the 20% additive pulsation for (c) $Re = 1200$.

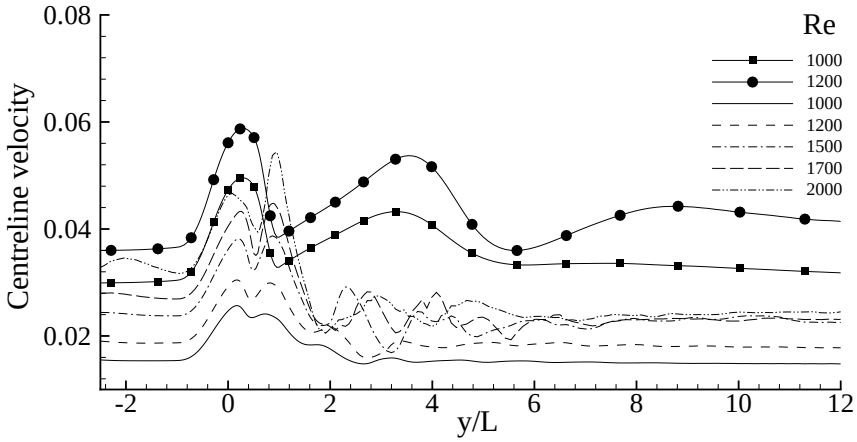

Figure 20: Mean centreline velocity for the different Reynolds numbers. The lines with symbols are the additive pulsatile results, while the lines without any symbols are the non-additive pulsatile results.

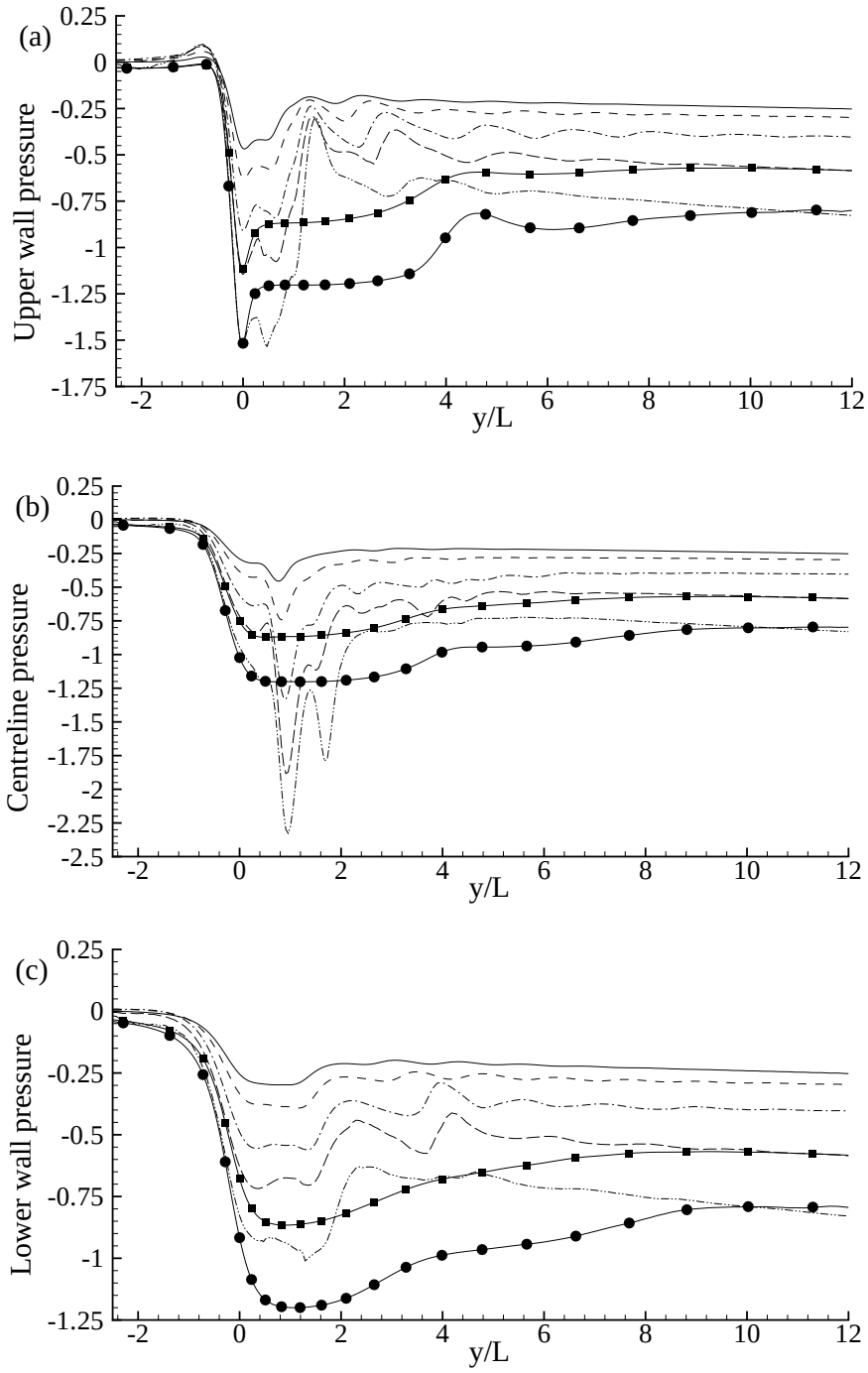

Figure 21: Mean pressure at the (a) upper wall, (b) centreline, and (c) lower wall for the different Reynolds numbers. For legend see Fig. 20.

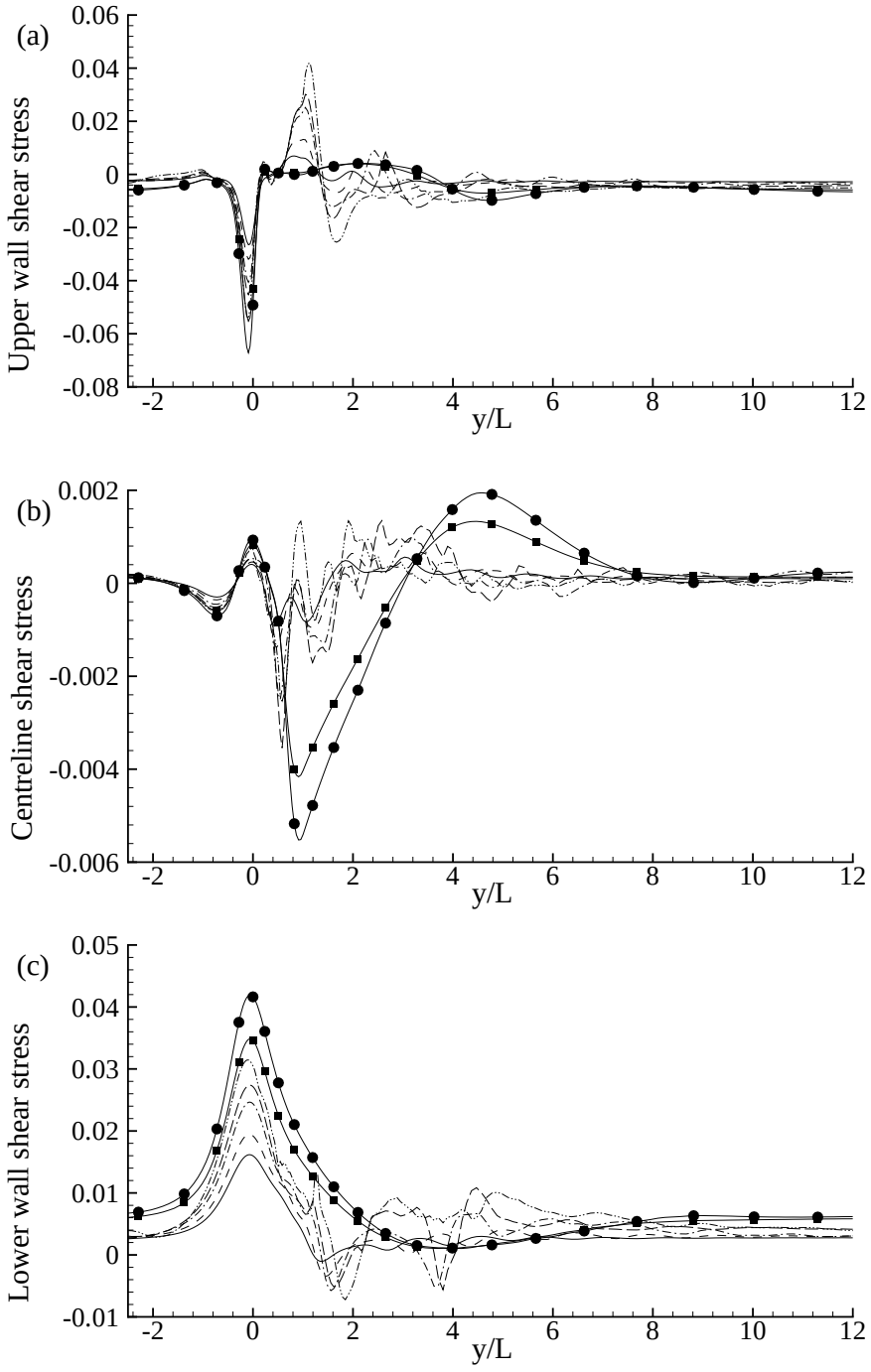

Figure 22: Mean shear stresses for the different Reynolds numbers at the (a) upper wall, (b) centreline, and (c) lower wall. For legend see Fig. 20.